NeuroImage: Clinical 30 (2021) 102675

Contents lists available at ScienceDirect

NeuroImage: Clinical

journal homepage: www.elsevier.com/locate/ynicl

In vivo tensor-valued diffusion MRI of focal demyelination in white and deep grey matter of rodents

Yi He [a,*], Susana Aznar [b], Hartwig R. Siebner [a,c,d], Tim B. Dyrby [a,e,*]

[a] Danish Research Centre for Magnetic Resonance, Centre for Functional and Diagnostic Imaging and Research, Copenhagen University Hospital Amager and Hvidovre, Copenhagen, Denmark
[b] Research Laboratory for Stereology and Neuroscience, Copenhagen University Hospital Bispebjerg and Frederiksberg, Copenhagen, Denmark
[c] Department of Neurology, Copenhagen University Hospital Bispebjerg and Frederiksberg, Copenhagen, Denmark
[d] Department for Clinical Medicine, Faculty of Health and Medical Sciences, University of Copenhagen, Copenhagen, Denmark
[e] Department of Applied Mathematics and Computer Science, Technical University of Denmark, Kgs. Lyngby, Denmark

ARTICLE INFO

Keywords:
Microscopic fractional anisotropy
Isotropic kurtosis
Tensor-valued diffusion
Metabolic alterations
Deep grey matter demyelination
DTI

ABSTRACT

Background: Multiple sclerosis (MS) is a chronic inflammatory demyelinating disease leading to damage of white matter (WM) and grey matter (GM). Magnetic resonance imaging (MRI) is the modality of choice to assess brain damage in MS, but there is an unmet need in MRI for achieving higher sensitivity and specificity to MS-related microstructural alterations in WM and GM.
Objective: To explore whether tensor-valued diffusion MRI (dMRI) can yield sensitive microstructural read-outs for focal demyelination in cerebral WM and deep GM (DGM).
Methods: Eight rats underwent L-α-Lysophosphatidylcholine (LPC) injections in the WM and striatum to introduce focal demyelination. Multimodal MRI was performed at 7 Tesla after 7 days. Tensor-valued dMRI was complemented by diffusion tensor imaging, quantitative MRI and proton magnetic resonance spectroscopy (MRS).
Results: Quantitative MRI and MRS confirmed that LPC injections caused inflammatory demyelinating lesions in WM and DGM. Tensor-valued dMRI illustrated a significant decline of microscopic fractional anisotropy (μFA) in both LPC-treated WM and DGM ($P < 0.005$) along with a marked increase of isotropic kurtosis (MK_I) in DGM ($P < 0.0001$).
Conclusion: Tensor-valued dMRI bears considerable potential for microstructural imaging in MS, suggesting a regional μFA decrease may be a sensitive indicator of MS lesions, while a regional MK_I increase may be particularly sensitive in detecting DGM lesions of MS.

1. Introduction

Demyelination of multiple sclerosis (MS) affects not only the white matter (WM) but also the cortex and deep grey matter (DGM) (Calabrese et al., 2015; Correale et al., 2017). The presence of focal grey matter lesions has been included as a diagnostic criterion, which is acknowledged in the latest diagnostic guidelines of MS, i.e., 2017 revisions of the McDonald criteria (Thompson et al., 2018). DGM involvement is associated with the progression of disability (Calabrese et al., 2012; Corral et al., 2019; Haider et al., 2014) and cognitive impairment (McKeithan et al., 2019). Magnetic resonance imaging (MRI) is the key mapping technique in MS (Ineichen et al., 2020; Nathoo et al., 2014; Reich et al., 2018), but there is an unmet need for higher sensitivity to disease-related microstructural changes, especially within cerebral grey matter (Bester et al., 2015; Chuhutin et al., 2019). Diffusion MRI (dMRI) offers high sensitivity to MS-related microstructural damage (Chu et al., 2019; Degaonkar et al., 2002; Le Bihan and Johansen-Berg, 2012; Lipp et al., 2020), yet the standard read-outs are heavily influenced by regional fiber orientation dispersion (e.g., crossing fibers), which hampers the detection of regional MS pathology (Andersen et al., 2020). This problem is not limited to standard diffusion tensor imaging (DTI) but also affects more advanced metrics if not accounting for fiber orientation dispersion effects.

Tensor-valued dMRI has been recently introduced as a method which can map microscopic fractional anisotropy (μFA) independent of complex fiber architecture, such as crossing and bending fibers (Jespersen

* Corresponding authors at: Danish Research Centre for Magnetic Resonance (DRCMR), Centre for functional and Diagnostic Imaging and Research, Copenhagen University Hospital Amager and Hvidovre, Kettegaard Alle 30, 2650 Copenhagen, Denmark.
E-mail addresses: yih@drcmr.dk, yi.he.mpi@gmail.com (Y. He), timd@drcmr.dk (T.B. Dyrby).

https://doi.org/10.1016/j.nicl.2021.102675
Received 17 January 2021; Received in revised form 22 March 2021; Accepted 24 March 2021
Available online 15 April 2021

et al., 2013, 2014; Kerkelä et al., 2020; Lasič et al., 2014; Lawrenz and Finsterbusch, 2019; Szczepankiewicz et al., 2016). The tensor-valued dMRI protocol decomposes the conventional total diffusion heterogeneity (referring to total Mean Kurtosis (MK_T)) signal at data acquisition into a microscopic anisotropy kurtosis (MK_A) and an isotropic kurtosis (MK_I) diffusivity component from which the μFA is estimated (Lasič et al., 2014; Nilsson et al., 2020; Szczepankiewicz et al., 2016; Westin et al., 2016). The MK_A indicates variances of anisotropic diffusivities at the microscopic scale dominated by sticks or cylindrical microstructures, such as neurites (dendrites or axons), whereas the MK_I reflects the variance of isotropic diffusivities or mean diffusivities in the microstructural environment (Nilsson et al., 2020; Szczepankiewicz et al., 2016). The MK_I is expected to be contributed by the restricted diffusion dominated by spherical compartments (such as cell bodies), the mean diffusivity components of axons, and isotropic diffusion in the extracellular space (Westin et al., 2016).

To validate the usefulness of tensor-valued dMRI metrics *in vivo*, animal models of MS may be used. A set of well-established MS animal models exists, including experimental autoimmune encephalomyelitis (EAE) (Aharoni et al., 2013; Battini et al., 2018; Chuhutin et al., 2019), cuprizone-diet (Guglielmetti et al., 2016; Jelescu et al., 2016; Oakden et al., 2017; Orije et al., 2015; Turati et al., 2015) and lysolecithin (LPC) injection model (Lassmann and Bradl, 2017; Nathoo et al., 2014; Ransohoff, 2012). Each model has specific strengths and weaknesses. LPC is an endogenous lysophospholipid that rapidly disrupts axonal myelin lipids and consistently induces local demyelination (Chu et al., 2019; Lehto et al., 2017; McCreary et al., 2009; Plemel et al., 2018). LPC triggers a robust local cellular immune response, causing demyelination (Ghasemlou et al., 2007; McMurray et al., 1993; Quinn et al., 1988). The LPC injection model allows the location of lesions to be freely chosen, and demyelination reaches a peak seven days after injections (Dousset et al., 1995; Jeffery and Blakemore, 1995; Lehto et al., 2017; Plemel et al., 2018). These properties motivated us to choose the LPC model, as it enabled us to induce localized demyelinating lesions in both WM and DGM, and to examine demyelination-induced microstructural changes already seven days after LPC injection.

In this study, we aimed to evaluate the potential of tensor-valued dMRI to capture focal MS-related microstructural damage in WM and DGM. We also compared with DTI and applied quantitative MRI to map local myelin content and proton magnetic resonance spectroscopy (MRS) to characterize changes at the neurochemical level.

2. Materials and methods

2.1. Focal demyelinating rodent model

All animal experiments were performed according to a protocol approved by Danish Animal Experiments Inspectorate (No. 2018-15-0201-01551) and in accordance with the guidelines of the European Communities Council Directive 2010/63/EU. Eight to nine-week-old male Sprague Dawley rats were injected with 1% L-α-Lysophosphatidylcholine (LPC, lysolecithin) provided by Sigma-Aldrich (L4129, Søborg, Denmark) to induce focal unilateral demyelination in both WM and DGM.

Saline was stereotactically injected in the contralateral hemisphere as intra-subject control. The two stereotactic injections used a nanoliter injector (WPI Inc., FL, USA) with a 33 gauge needle and targeted both the external capsule (EC) and caudate-putamen (CPu). To ensure demyelination in both EC and CPu regions, we injected LPC at five different depths between EC to CPu, as illustrated in Fig. 1(a). Stereotactic coordinates for LPC were: Anterior/Posterior (AP) = 0.04 mm; Medial/Lateral (ML) = 2.8 mm; Dorsal/Ventral (DV) = 5.0 mm, 4.5 mm, 4.0 mm, 3.5 mm (CPu), and 3.0 mm (EC). The contralateral injection sites of the saline were the same as those of LPC except for ML = −2.8 mm (Fig. 1(a)). There were visible effects of the saline injections in some of the rats (as the red arrows in Supplementary Fig. 1), whereas some of the rats recovered completely after seven days of saline injections. At each hemisphere, the injection volume at each of the five depths was 1 μl, and the rate of injection was 0.1 μl/min controlled by the nanoliter injector. At the last injected site of both LPC and saline, the needle was

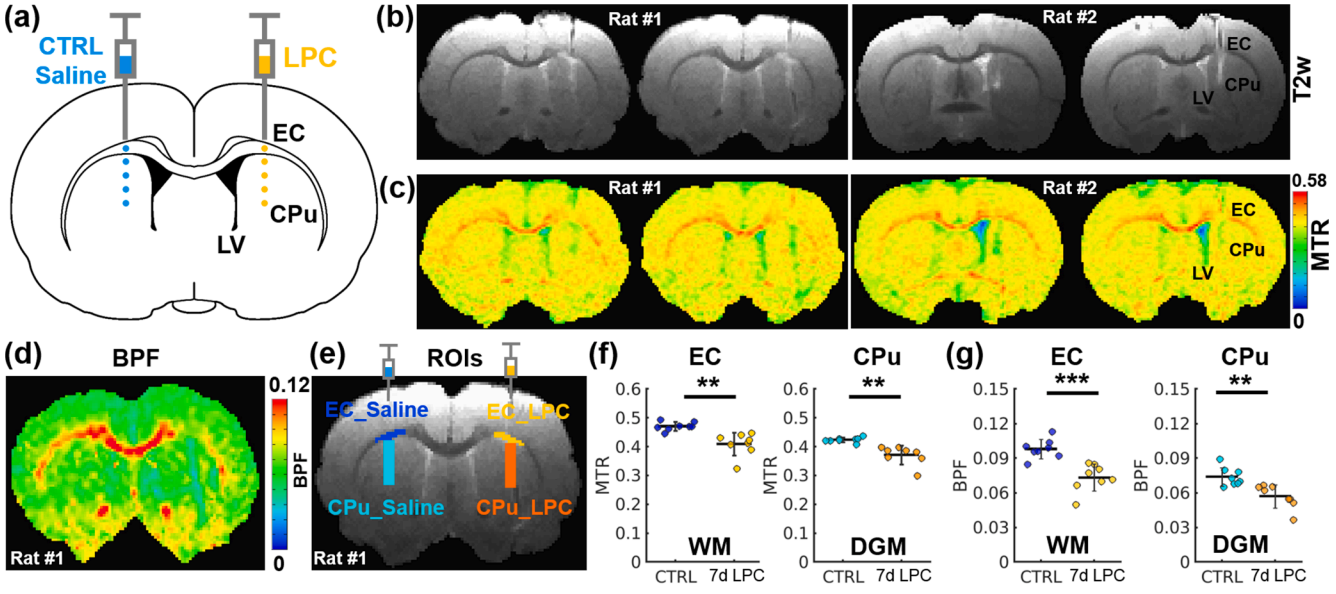

Fig. 1. Decreased MTR and Myelin-sensitive BPF in both LPC-treated WM external capsule (EC) and DGM caudate putamen (CPu). (a) Focal demyelinating rodent model. (b) Representative T2-weighted (T2w) images from Rat #1 and Rat #2 on seven days post LPC treatment (7d LPC). (c) Representative MTR images from Rat #1 (Left) and Rat #2 (Right) (d) Myelin-sensitive BPF from Rat #1. (e) ROIs in the representative Rat #1 (EC_Saline: blue, EC_LPC: yellow, CPu_Saline: cyan, and CPu_LPC: orange). (f) Left: group plots of MTR from WM EC of CTRL saline and DGM LPC treatment (**$P = 0.0046$, n = 8 rats, paired *t*-test, mean ± SD, CTRL (blue): 0.472 ± 0.015, 7d LPC (yellow): 0.410 ± 0.039); Right: MTR of CPu from CTRL saline and LPC injections (**$P = 0.0016$, CTRL (cyan): 0.425 ± 0.008, 7d LPC (orange): 0.372 ± 0.033). (g) Left: a significant reduction of BPF from LPC-treated WM (***$P = 0.0008$, CTRL saline: 0.098 ± 0.008, 7d LPC: 0.073 ± 0.012); Right: decreased BPF in CPu lesions of LPC (**$P = 0.0021$, CTRL saline: 0.074 ± 0.008, 7d LPC: 0.057 ± 0.010). Significant alterations are represented as **$P < 0.005$ and ***$P < 0.001$. All error bars represent SD. (For interpretation of the references to colour in this figure legend, the reader is referred to the web version of this article.)

kept in the brain for 10 min before removing it slowly. Demyelination was evaluated seven days after post operations, and all rats underwent in-vivo MRI scans.

2.2. In vivo MRI acquisition and analysis

All *in vivo* MRI experiments were performed on a 7.0 T Bruker Biospec preclinical MRI system equipped with a maximum gradient strength of 660 mT/m and a 20 mm inner diameter receive-only surface coil combined with an 86 mm inner diameter transmit-only resonator (Bruker BioSpin, Ettlingen, Germany).

Rats were initially anesthetized with 5% isoflurane for about 5 min and maintained with 1.5–2.5% isoflurane mixed with air and oxygen throughout the experiment. The body temperature was monitored with a rectal probe and maintained at 37 °C by a feedback-regulated warm airflow. Respiration rate was monitored using an MR-compatible monitoring system (PC-SAM, Small Animal Instruments Inc., Stony Brook, NY, USA). All rats with injections were examined on seven days post LPC treatment (7d LPC). The imaging protocols included a high-resolution T2-weighted structural MRI for visualization purposes, two myelin-related imaging protocols, microstructure anisotropy imaging used tensor-valued dMRI and finally, metabolic spectra acquired by proton MRS. Two myelin-related protocols contained the clinically widely used magnetization transfer ratio (MTR) imaging and a quantitative mapping myelin-sensitive bound pool fraction (BPF) imaging.

2.2.1. T2-weighted (T2w) images

A rapid acquisition with relaxation enhancement (RARE) sequence acquired high-resolution T2w imaging (Fig. 1(b)) with the following parameters: repetition time (TR): 3200 ms; echo time (TE): 30.6 ms; matrix size: 256 × 256; field of view (FOV): 36 × 36 mm^2; slice thickness: 0.4 mm, 17 coronal slices; RARE factor: 8; and total acquisition time: 10 min.

2.2.2. Tensor-valued dMRI

A multi-shot spin-echo echo-planar imaging (EPI) sequence with a free diffusion encoding gradient waveform implementation was used to acquire tensor-valued diffusion MR images. The tensor-valued dMRI included a Linear Tensor Encoding (LTE) protocol and a Spherical Tensor Encoding (STE) protocol. The gradient waveforms of LTE and STE comprised two blocks of 16 ms diffusion waveform encodings placed before and after the refocusing pulse (Fig. 2(a)) (Lasič et al., 2014; Lundell et al., 2019; Szczepankiewicz et al., 2016). We used a tuned waveform design to match the diffusion time of the two acquisitions (Lundell et al., 2019). For translational comparison, the same four b-values as implemented *in vivo* humans (Szczepankiewicz et al., 2019) were implemented for both LTE and STE: 200, 700, 1400, and 2000 s/mm^2. The acquisition parameters were: TE = 46.5 ms; TR = 3500 ms; in-plane resolution of 250 × 250 μm^2; number of segments = 16; slice thickness = 400 μm. STE was repeated the same as the number of LTE directions at each b value and averaged offline. The total acquisition time of LTE and STE tensor-valued dMRI was 90 min. Powder averaging (averaging all directional image volumes per b-value) was applied to each b-value shell of LTE for obtaining a fiber orientation-invariant diffusion signal (Afzali et al., 2020; Edén, 2003; Yablonskiy et al., 2002). From the powder averaging of the LTE acquisitions and the averaged STE acquisitions, a set of microstructural metrics without the effect of fiber orientation dispersion were calculated by using the online MD-dMRI Matlab toolbox (https://github.com/markus-nilsson/md-dmri). Here the total mean total kurtosis (MK_T) and the mean isotropic kurtosis (MK_I) were calculated by fitting the respective signal decay curves of the powder averaged LTE and the STE acquisitions. The sum of MK_I and the mean anisotropic kurtosis (MK_A) is MK_T. The microscopic fractional anisotropy (μFA) (Fig. 3) is estimated from MK_I and MK_A (Lasič et al., 2014; Szczepankiewicz et al., 2016). The powder averaged LTE, and the STE signal decays, as well as the derived metrics in different brain regions of interest (ROIs) is demonstrated from one representative rat without operations (Supplementary Fig. 2).

2.2.3. Traditional diffusion tensor imaging

A pulsed gradient spin echo (PGSE) sequence with EPI acquisition was implemented for diffusion tensor imaging (DTI). The sequence parameters are as follows: TE, 30 ms; TR: 3500 ms; Gradient duration (δ), 4 ms; Gradient separation (Δ), 10 ms; 42 non-collinear directions (Jones, 2004; Jones et al., 1999) with b value 1400 s/mm^2 and 3 non-diffusion weighted images (b = 0 s/mm^2); 250 × 250 μm^2 in-plane image

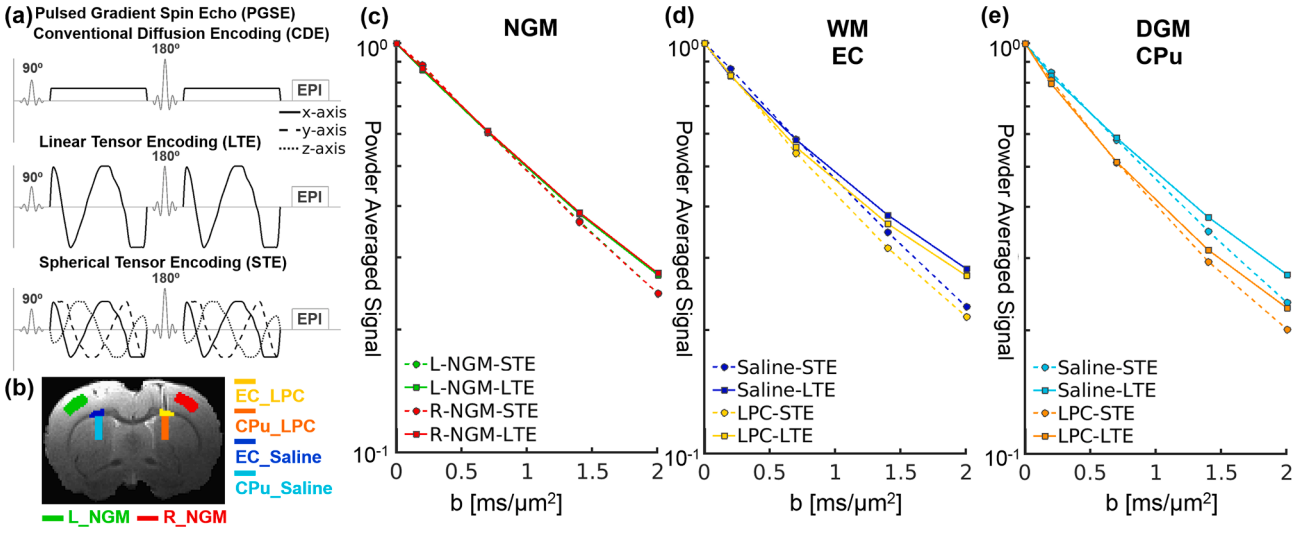

Fig. 2. Gradient waveforms and powder averaged signal of tensor-valued diffusion MRI (a) A pulsed gradient spin-echo (PGSE) for DTI (Top), a tuned linear tensor encoding (LTE, Middle) and a spherical tensor encoding (STE, Bottom) waveform (Lundell et al., 2019) (b) A representative coronal slice with the ROIs (Yellow ROI: external capsule (EC) lesions of LPC treatment; Orange, deep gray matter (DGM) caudate-putamen (CPu) lesions of LPC injections; Blue, EC ROI of saline treatment; Cyan: CPu ROI of saline injections; Green: Left ROI of normal gray matter (NGM); Red: Right ROI of NGM (c) Powder averaged signal decays of LTE and STE from the left and right ROIs of NGM (d) Powder averaged signal decays of LTE and STE from the WM EC ROIs of 7d LPC and saline injections (e) Powder averaged signal of LTE and STE from the DGM CPu with 7d LPC and saline treatment. (For interpretation of the references to colour in this figure legend, the reader is referred to the web version of this article.)

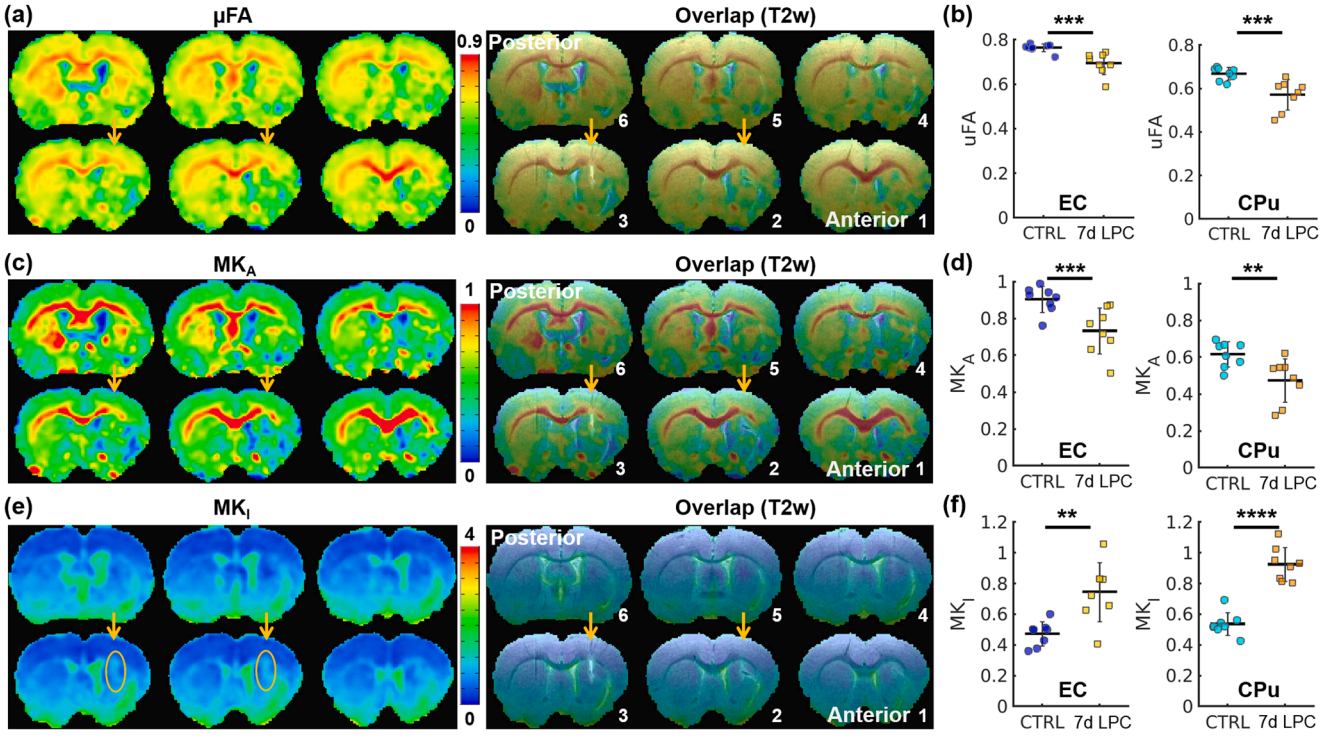

Fig. 3. Tensor-valued diffusion MRI metrics of WM EC and DGM CPu lesions (a) Left: tensor-valued diffusion MRI metric μFA images; Right: μFA images were overlaid top of T2w images (yellow arrows denote the location of LPC injections). (b) Left: a significant reduction of μFA in WM EC lesions with LPC treatment (***P = 0.0028, paired t-test, n = 8 rats, mean ± SD, CTRL saline: 0.766 ± 0.018, 7d LPC: 0.696 ± 0.050); Right: decreased μFA in DGM CPu lesions of LPC injections (***P = 0.002, CTRL: 0.670 ± 0.029, 7d LPC: 0.573 ± 0.070); (c) Left: tensor-valued diffusion MRI metric anisotropic kurtosis (MK_A) maps; Right: MK_A maps were overlaid top of T2w images. (d) Left: a significant decrease of MK_A in LPC-treated WM EC (***P = 0.0033, CTRL, 0.905 ± 0.071, 7d LPC: 0.734 ± 0.125); Right: MK_A in DGM CPu lesions of CTRL and LPC treatment (**P = 0.0051, CTRL, 0.617 ± 0.068, 7d LPC: 0.475 ± 0.119); (e) Left: tensor-valued diffusion MRI metric isotropic kurtosis (MK_I) images; Right: transparent MK_I images with T2w images. (f) Left: MK_I values of EC in CTRL saline ROI and LPC ROI (**P = 0.0055, CTRL: 0.475 ± 0.079, 7d LPC: 0.748 ± 0.192); Right, a dramatical increase of MK_I from DGM CPu lesions of LPC treatment (****P = 0.000023, CTRL: 0.538 ± 0.074, 7d LPC: 0.927 ± 0.111). Significant changes are represented as *P < 0.05, **P < 0.01, ***P < 0.005, ****P < 0.0001. Yellow arrows indicate the sites of LPC injections, and all error bars represent SD. (For interpretation of the references to colour in this figure legend, the reader is referred to the web version of this article.)

resolution and 400 μm slice thickness; 8 segments and 21 mins total scan time. The matrix size is 144 × 144 as the same in tensor-valued dMRI. The DTI metrics, i.e., the fractional anisotropy (FA), mean diffusivity (MD), axial diffusivity (AD), radial diffusivity (RD) were estimated using the MRtrix3 tool (https://www.mrtrix.org/).

2.2.4. Magnetization transfer ratio (MTR)

A fast low angle shot magnetic resonance imaging (FLASH) sequence with and without magnetization transfer (MT) saturation pulse was acquired using the parameters: TR = 450 ms, TE = 2.8 ms, flip angle = 20°, matrix size = 256 × 256, FOV = 36 × 36 mm^2, total acquisition time = 15 min, 17 coronal slices, and 0.4 mm slice thickness. The MT saturation pulse was used with Gaussian shape, peak power 7.5 μT, duration 15 ms, and frequency offset 1500 Hz. An MTR image was then calculated as $MTR = (MT_{off} - MT_{on})/MT_{off}$, as shown in Fig. 1(c).

2.2.5. Quantitative MT imaging

A 2D selective inversion-recovery prepared fast spin-echo sequence (Gochberg and Gore, 2007) was implemented to acquire a single coronal slice of quantitative MT data to derive the myelin-sensitive Bound Pool Fraction (BPF). The sequence had the following parameters: TE = 6 ms, Echo Train = 16, Matrix = 144 × 144, in-plane resolution = 250 × 250 $μm^2$, the coronal slice covered the injection site with slice thickness = 0.4 mm. The sequence was repeated 21 times with inversion times log-spaced from 3.5 to 10000 ms. Total acquisition time = 43 min. Prior to Fourier image reconstruction, k-space data for all images were apodized using a Tukey window with a 0.25 taper-to-window ratio and zero-padding, resulting in 125 μm nominal in-plane resolution. The BPF was estimated from the equilibrium magnetizations of the free pools M_{0f}, and the bound pools M_{0b} as $BPF = M_{0b}/(M_{0b} + M_{0f})$. The longitudinal relaxation and magnetization transfer between water (M_{0f}) and macromolecular protons (M_{0b}) (West et al., 2018) were calculated by fitting the series of inversion time images to the Bloch-McConnell equations. Both MRI sequences and Matlab codes are available online (https://remmi-toolbox.github.io/).

2.2.6. Proton magnetic resonance spectroscopy (^{1}H-MRS)

In vivo localized ^{1}H MRS was acquired by using a point resolved spectroscopy sequence (PRESS): TR/TE = 2500/34 ms, voxel size = 2 × 2 × 2 mm^3, spectral width = 3000 Hz, acquisition point = 2048, 192 averages, and 8 min acquisition time. The water signal was suppressed with the variable power RF pulses with optimized relaxation delays (VAPOR) scheme combined with outer volume saturation (OVS). *In vivo* proton spectra (Fig. 4(a)) were analyzed using an automated deconvolution program (LCModel (Provencher, 2001)). The LCModel analysis was performed in the chemical shift range of 0.2–4.0 ppm. The basis set of LCModel includes alanine (Ala), aspartate (Asp), creatine (Cr), γ-aminobutyric acid (GABA), glucose (Glc), glutamine (Gln), glutathione (GSH), glutamate (Glu), glycerophosphorylcholine (GPC), Myo-inositol (Ins), lactate (Lac), N-acetylaspartate (NAA), N-acetylaspartylglutmate (NAAG), phosphorylcholine (PCh), phosphocreatine (PCr), scyllo-inositol (sIns) and taurine (Tau). The sums of some metabolites are expressed as total choline-containing compounds (GPC + PCh or tCho), total NAA (NAA + NAAG or tNAA) and tCr (Cr + PCr) (Fig. 4(b)-(c)). The Cramer-Rao lower bounds (CRLB) provided by LCModel were used to assess the reliability of the metabolite quantification. The

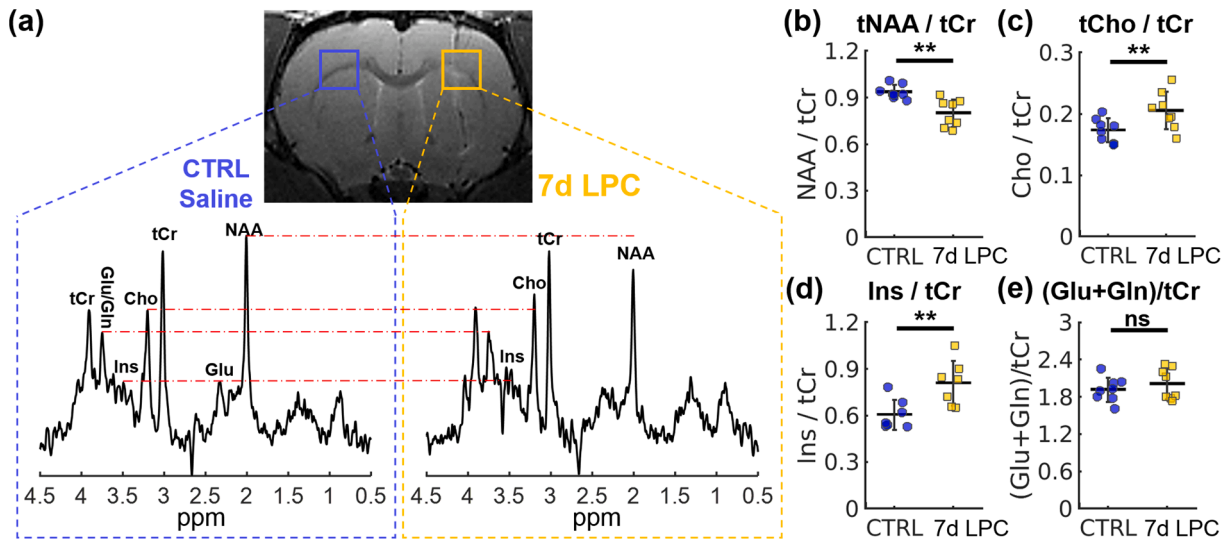

Fig. 4. Metabolic alterations in lesions with LPC treatment (a) Two volumes of interest (VOIs) were positioned in the coronal T2w image (Left: CTRL saline; Right: 7d LPC). The corresponding proton spectra of the two VOIs demonstrate metabolite peaks at different chemical shifts. (b) The metabolite ratio tNAA / tCr of LPC VOI was significantly lower than that of CTRL saline VOI (**$P = 0.0024$, paired t-test, n = 8 rats, mean ± SD, CTRL, 0.939 ± 0.045, 7d LPC, 0.803 ± 0.089). (c) A significant increase of the metabolite ratio tCho / tCr from LPC spectra (**$P = 0.0012$, CTRL: 0.174 ± 0.019, 7d LPC: 0.206 ± 0.030). (d) Increased the ratio Ins / tCr from the spectra of LPC lesions (**$P = 0.0029$, CTRL: 0.607 ± 0.098, 7d LPC: 0.811 ± 0.143). (e) There is no significant difference in the metabolisms ratio (Glu + Gln)/tCr from the VOI of LPC lesions and that of CTRL (ns, $P > 0.05$, no significant differences, CTRL: 1.923 ± 0.195, 7d LPC: 2.017 ± 0.251). All error bars represent SD, and significant differences are as **$P < 0.005$.

metabolites with CRLB ≤20% were quantified for further statistical analysis.

2.3. Histological examination

One ex-vivo brain was fixed in 4% formalin for histological examination. The brain was then cut in a vibratome into 50-μm-thick sections, mounted on gelatine-coated slices, and after air-dried, stained with hematoxylin and eosin (H&E) (Cardiff et al., 2014). The details of H&E stain are as follows: samples were stained with a hematoxylin solution for 4 min, and then placed under running tap water for 10 min; samples were then stained in eosin Y solution for 1 min followed by dehydration in 95% and 100% ethanol for 5 min; finally, the slides were submerged in xylene for 5 min and cover-slipped with Pertex mounting medium. The slides were visualized with an Olympus BX 50 microscope (Olympus, Denmark). Digital images were created, and the number of cell nuclei was counted on selected ROIs by use of the ImageJ software from the NIH (http://rsbweb.nih.gov/ij/download.html).

2.4. Statistics

Paired t-tests were performed to compare MRI metrics of LPC ROIs with those of control (CTRL) ROIs. The ROIs of the lesions were defined manually by ITK-SNAP software (http://www.itksnap.org/) (Fig. 1(e)). The P values <0.05 were considered statistically significant. Stars indicate significant differences, while 'ns' denotes no significant comparisons. All error bars indicate the standard deviation (SD).

3. Results

3.1. A reduction of μFA (microstructural anisotropy) and increased MK_I in WM and DGM lesions

We first inspected the signal decays of powder averaged LTE and the STE acquisitions for both saline and LPC treatment. We selected two normal cortical regions bilaterally (Fig. 2(b)), demonstrating no difference between the powder averaged signal of these two regions (Fig. 2(c)). In the cerebral white matter, we observed the slowest powder averaged signal decay curve of LTE in saline-treated EC (solid blue line in Fig. 2(d)) and a slightly faster LTE decay curve of LPC-treated EC (solid yellow line in Fig. 2(d)). Similar trends were illustrated in the signal decays of STE with saline and LPC treatment (Fig. 2(d), blue and yellow dash lines). In the DGM CPu ROIs, the powder averaged signal decay curves of LTE and STE are closer than that from WM EC for both saline and LPC treatment, suggesting a dominating cellular environment in DGM CPu (Saline: dash vs. solid cyan lines; LPC: dash vs. solid orange lines in Fig. 2(e)). Interestingly, the STE signal decay curve in CPu lesions with saline treatment (dash cyan line) is even slower than that of LTE in LPC-treated CPu (solid orange line) (Fig. 2(e)).

In both WM and DGM, the μFA was significantly decreased in lesions with LPC treatment as compared to that of saline controls (Fig. 3(a-b), EC: ***$P = 0.0028$, CPu: ***$P = 0.002$, paired t-test, n = 8 rats). The MK_A showed significant decline in both LPC-treated EC and CPu compared to saline (Fig. 3(c-d), EC: ***$P = 0.0033$, CPu: **$P = 0.0051$). In the CPu ROI, we found a substantial increase in MK_I after LPC treatment (Fig. 3(e-f), ****$P = 0.000023$, paired t-test, n = 8 rats, mean ± SD, CTRL saline: 0.538 ± 0.074, LPC: 0.927 ± 0.111) but also in the LPC treated EC (**$P = 0.0055$, CTRL Saline: 0.475 ± 0.079, LPC: 0.748 ± 0.192). In all rats, the MK_I value in the CPu ROI was higher in the LPC-treated hemisphere than the respective MK_I values in the placebo-treated hemisphere.

To assess the performance of tensor-valued dMRI metrics in discriminating LPC and saline-treated lesions, we implemented receiver operating characteristic (ROC) analysis to calculate the area under the ROC curve (AUC) (Supplementary Fig. 3). Higher AUC values represent better performance in discriminating LPC-treated lesions with controls. The ROC of μFA demonstrated high AUC values in separating LPC-induced WM lesions from saline-treated WM (Supplementary Fig. 3, AUC WM: 0.953, n = 8 rats), and also a high AUC of μFA was observed in DGM (AUC DGM: 0.969 for saline vs. LPC). The AUC values of MK_A in both WM and DGM were slightly lower than those of μFA, but still illustrated good discrimination ability (AUC WM: 0.906 for saline vs. LPC, and AUC DGM: 0.891). Similarly, we also observed a high AUC of MK_I in WM (AUC WM: 0.906). Notably, MK_I demonstrated the best performance in distinguishing LPC-induced DGM lesions with saline-treated DGM lesions (Supplementary Fig. 3, AUC GM: 1, n = 8 rats).

We also derived the DTI metrics (Supplementary Fig. 4) and assessed the performance of the DTI metrics in discriminating LPC and saline-induced lesions (Supplementary Fig. 5). In line with previous DTI studies (Chu et al., 2019; DeBoy et al., 2007; Degaonkar et al., 2002; Fujiyoshi et al., 2016; Luo et al., 2019; Tourdias et al., 2011), the fractional anisotropy (FA) values in the demyelinating lesions were also significantly decreased (Supplementary Fig. 4(a-b), paired *t*-test, n = 8 rats, WM EC, ****P = 0.00006; DGM CPu, ***P = 0.0009). However, the performance of FA in discriminating LPC and saline-treated lesions was lower than μFA (Supplementary Fig. 5(a) and Supplementary Table 1, AUC WM of FA: 0.844 vs. AUC WM of μFA: 0.953; AUC DGM of FA: 0.938 vs. AUC DGM of μFA: 0.969). Moreover, MD showed the best performance in all DTI metrics for separating the LPC and saline-induced lesions in DGM but was still inferior to the tensor-valued diffusion metric MK_I (AUC DGM of MD: 0.938 vs. MK_I: 1, Supplementary Table 1–2). The crossing fibers regions between the corpus callosum and cingulum bundles demonstrated low FA but high μFA values, clearly illustrating that FA is sensitive to fiber orientated dispersion, but not μFA (Supplementary Fig. 6).

3.2. Decreased MTR and Myelin-sensitive BPF in both WM and CPu of LPC treatment

LPC treatment led to a reduction of MTR in both WM EC and DGM CPu (Fig. 1(b-c, f), $^{**}P < 0.005$, n = 8 rats, paired *t*-test), recapitulating similar observations of myelin loss in EAE (Aharoni et al., 2013) and cuprizone-treated (Turati et al., 2015) animal models. The MTR metric is known to be biased by T1-relaxation changes due to demyelination (Helms et al., 2008). Thus we derived the myelin-sensitive BPF to quantify demyelination (Fig. 1(d)). Quantitative BPF values in WM lesions of LPC treatment were decreased seven days post-operation (Fig. 1(g), Left, $^{***}P < 0.001$, n = 8 rats, paired *t*-test, CTRL: 0.098 ± 0.008, LPC: 0.073 ± 0.012). Similarly, a significant decrease in BPF was also observed in CPu after LPC injection (Fig. 1(g), Right, $^{**}P < 0.005$). Hence, quantitative BPF supported the MTR findings but showed increased sensitivity to demyelination in WM lesions.

3.3. Metabolic alterations in lesions of LPC treatment

We used ^{1}H MRS to characterize metabolic alterations of LPC-treated lesions (Fig. 4(a)). The metabolite ratio tNAA/tCr was significantly decreased in the VOIs after LPC injections (Fig. 4(b), $^{**}P = 0.0024$, paired *t*-test, n = 8 rats, mean ± SD, CTRL Saline, 0.939 ± 0.045, LPC, 0.803 ± 0.089), in agreement with EAE (Battini et al., 2018) and cuprizone (Orije et al., 2015) animal studies. Compared with the VOI of control saline, increased levels of the metabolite ratio tCho/tCr were observed in LPC-treated lesions (Fig. 4(c), $^{**}P = 0.0012$, n = 8 rats, CTRL: 0.174 ± 0.019, LPC: 0.206 ± 0.030), interpreting increased membrane turnover associated with inflammatory cellular infiltration (Davie et al., 1994). Similarly, we also found that LPC treatment boosted the ratio Ins/tCr (Fig. 4(d), $^{**}P = 0.0029$, n = 7 rats, CTRL: 0.607 ± 0.098, LPC: 0.811 ± 0.143), indicating glial activation and proliferation in the lesions (Brand et al., 1993). The metabolite ratio (Glu + Gln)/tCr did not show any significant changes in the VOIs of LPC injections (Fig. 4(e), $P > 0.05$, paired *t*-test, n = 8 rats, mean ± SD, CTRL: 1.923 ± 0.195, LPC: 2.017 ± 0.251).

4. Discussion

This is the first study showing that μFA and the decomposed kurtosis metrics (MK_I and MK_A) can capture LPC-induced focal demyelination effects in the WM and DGM. The tensor-valued dMRI metrics illustrated better performance than traditional DTI metrics in separating LPC and saline-treated lesions which may be explained by its independence to the confounding fibre orientation dispersion effect (Supplementary Fig. 6) (Andersen et al., 2020; Lehto et al., 2017). The focal demyelination induced by LPC treatment caused a consistent decrease in regional μFA (Fig. 1(b–d) vs. Fig. 3(a)), supporting our recent findings in MS patients (Andersen et al., 2020).

How can this decrease in μFA be interpreted? μFA will be reduced, if demyelination and resulting neuroinflammation reduce the ratio between anisotropic versus isotropic diffusion processes, e.g., the density of axons (cylinders) versus the density of cell bodies or free diffusion (spherical shapes). If neurite bundles are straight and aligned, then μFA is expected to be the same as FA. However, neurites are rarely straight and aligned, and can cross as well which can reduce FA but not the μFA (Supplementary Fig. 6) (Abdollahzadeh et al., 2019; Andersen et al., 2020; Andersson et al., 2020; Lasič et al., 2014; Lee et al., 2020; Shemesh, 2018; Szczepankiewicz et al., 2015). In our LPC-injection model of focal demyelination, we argue that both, a decreased volume fraction of anisotropic diffusion and an increased volume fraction of isotropic diffusion processes, contributed to a decrease in μFA in both WM and GM lesions. In MS lesions, transmission electron microscopy and two-photon fluorescence microscopy of LPC treatment have illustrated myelin and axonal spheroids (Lehto et al., 2017; Plemel et al., 2018), likely resulting in an increased volume fraction and variances of isotropic diffusivities. On the other hand, the decreased MTR and BPF indicated a reduction of myelin content (Fig. 1(c–g)), inducing the decreased volume fraction of anisotropic diffusion. Furthermore, NAA is synthesized in the mitochondria of neurons and axons (Moffett et al., 2007). A previous histological study also demonstrated a decrease of NAA and a relatively reduced axonal density in demyelinating lesions, supporting NAA as an indicator of axonal integrity (Bitsch et al., 1999). The reduction of NAA in our MRS results (Fig. 4(b)) reflects axon injury and loss, indicating a decrease of axonal density in LPC-treated lesions. The increased Ins suggested glial activation in LPC treated lesions, further enhancing the volume fraction and possible variation in isotropic diffusivities. Collectively, the decreased ratio between anisotropic and isotropic diffusivities can explain the observed reduced μFA in both LPC-treated WM and DGM.

The μFA metric is derived from the combination of MK_A and MK_I metrics, integrating the contributions of both anisotropic and isotropic diffusion processes (Lasič et al., 2014; Szczepankiewicz et al., 2016). Receiver operating characteristic (ROC) analysis demonstrated that μFA has a high performance and sensitivity in discriminating LPC treated WM and controls, and similar performance was observed in DGM lesions (Supplementary Fig. 3 and Table 2). Similarly, MK_A detects microscopic anisotropy, presenting a higher sensitivity in distinguishing WM lesions comparing with DGM lesions (Supplementary Table 2). Supportively, MK_A demonstrates that neurites microstructure anisotropy is higher in densely packed WM axons, whereas lower anisotropy in GM (Fig. 3(c)). In contrast, MK_I illustrated a very good performance and sensitivity in DGM lesions (Supplementary Fig. 3 and Table 2).

Interestingly, the isotropic kurtosis (MK_I) showed a prominent change in the putamen after LPC-treatment relative to placebo, making this metric a promising candidate read-out for the future detection of MS-related involvement in DGM (Supplementary Fig. 3 and Table 2). The MK_I metric has the technical advantage of being sensitive to the variance of spherical-liked shaped microstructures (i.e., cell bodies, vacuoles), indicating variable cell density or a mixture of tissue compartments (Szczepankiewicz et al., 2015, 2016; Westin et al., 2016). In previous studies, histological images have demonstrated that MK_I was associated with cell density variance (Nilsson et al., 2020; Szczepankiewicz et al., 2016). There are several contributions to the significantly increased MK_I in LPC-treated CPu lesions (Fig. 3(e-f)). Firstly, vacuoles and myelin debris, observed by transmission electron microscopy (Lehto et al., 2017), boost the variance of tissue mixtures. Our H&E stain results demonstrated more cellular nuclei in LPC treated lesions, suggesting cell proliferation/infiltration associated with inflammation (Supplementary Fig. 7). Moreover, the previous immunofluorescence staining studies reported a proliferation of oligodendrocyte precursor cells (OPCs) already 3–7 days post LPC treatment

(Lau et al., 2012; Shi et al., 2018; Yazdi et al., 2015). The OPCs recruitment may also increase the variance of cells, contributing to the increase of MK_I. The increased Ins levels in our MRS results (Fig. 4(d)) also indicated microglia and astrocyte activation in LPC lesions (Chu et al., 2019). The cell proliferation/infiltration in LPC induced lesions increases cell density as well as the variability in cell sizes and shapes. Hence, we attribute the increase in putaminal MK_I to changes in the density variance of spherical-shaped anatomical features in GM structures. This finding highlight the role of MK_I in detecting GM lesions and potentially fulfilling dissemination in space of MS lesions.

Quantitative MRI (qMRI) and ^{1}H-MRS validated the tensor-valued dMRI results, showing that LPC-treatment did induce structural and metabolic changes that are characteristic of a focal demyelinating brain lesion. Since BPF and MTR are highly correlated with histological measures of myelin content (Heath et al., 2018; West et al., 2018), our findings confirm that LPC treatment induce focal demyelination in both WM and DGM CPu and not in the saline-injected hemisphere. The demyelination in both LPC treated WM and DGM CPu contributed to decreased μFA and MK_A. Complementing myelin content related qMRI, ^{1}H-MRS assessed brain metabolism to interpret microstructural alterations induced by LPC treatment. Our ^{1}H MRS results demonstrated a reduction of tNAA and increased tCho and Ins, which also have been reported in MS patients (Fleischer et al., 2016; Hnilicová et al., 2019). Our ^{1}H MRS findings suggested that LPC treatment leads to inflammation and glial activation in lesions. Moreover, cell proliferation/ infiltration was observed in the LPC treated lesions from our H&E stain results (Supplementary Fig. 7). Together, these data corroborated the induction of inflammatory demyelination in LPC-treated lesions and provided myelin-related and metabolic information to interpret the alterations of μFA and MK_I. The tensor-value MRI metrics reflect microscopic diffusion anisotropy and isotropy processes of microstructural environments with a higher spatial image resolution than MRS, and better specificity to the changes of cell shapes and cell density than MTR and BPF.

Low signal-to-noise ratio (SNR) affects accuracy and precision of diffusion metrics (Jones and Basser, 2004; McClymont et al., 2017). To evaluate the SNR effects on our tensor-valued dMRI results, we calculated the SNR maps of healthy and demyelinated lesions at each b-value of both STE and LTE (Supplementary Fig. 8). The previous study simulated the precision of tensor-valued dMRI metrics affected by signal noise level (Szczepankiewicz et al., 2019), demonstrating that MK_I, MK_A, and μFA have no strong positive bias when SNR values at $b = 0$ s/mm^2 images are >20. Here, the SNR values of both LTE and STE at $b = 0$ s/mm^2 are higher than 40 at both healthy and demyelinated lesions (Supplementary Fig. 8(b) & (g)), suggesting neglected noise-induced biases in our results.

Here we applied a tensor-valued dMRI protocol to map μFA that takes advantage of combining two types of diffusion encodings with different shapes of the b-tensor, i.e., LTE and STE, respectively (Nilsson et al., 2020; Szczepankiewicz et al., 2016). Other dMRI approaches also attempt to disentangle fiber orientated dispersion from microstructure features, but they all used a single diffusion encoding scheme (i.e., PGSE) such as the spherical-mean technique (Kaden et al., 2016), neurite density diffusion imaging (NODDI) (Zhang et al., 2012), or many more (Alexander et al., 2019). By combining different shapes of b-tensor encodings, tensor valued dMRI can disentangle a compartment signal already at the acquisition stage, reducing the need for more advanced mathematical models and model assumptions often required for the single diffusion encoding methods (Lampinen et al., 2017; Lundell et al., 2019; Novikov et al., 2019; Yon et al., 2020).

Our study does have limitations. 3D histopathological validation may enable a better interpretation of the tensor-valued dMRI metrics μFA and MK_I. This will be pursued in a future study in which we will utilize synchrotron radiation phase-contrast tomography (Andersson et al., 2020) with an isotropic nanoscale resolution to elucidate a 3D ground truth (tissue microstructure of MS). Furthermore, future studies should also link brain function with microstructural alterations reflected by μFA and MK_I. This will be possible by implementing simultaneous functional MRI and intracellular calcium recording (He et al., 2018) in the MS model, investigating the relation between μFA and MK_I changes with impaired function at the cellular and global brain scale.

5. Conclusions

We characterize an LPC-treated demyelinating rodent model with defined WM and DGM lesions using multimodal MRI (quantitative myelin-sensitive BPF mapping, tensor-valued dMRI, conventional DTI, and ^{1}H-MRS). Tensor-valued dMRI metric μFA demonstrates a significant reduction in both WM and DGM lesions. Meanwhile, the MK_I metric achieves high performance in LPC treated DGM lesions due to changes in the density variance of spherical shaped anatomical features, i.e., inflammation processes. Our findings suggest μFA may be a promising biomarker of both WM and GM lesions, whereas MK_I may be particularly suited for GM lesions in MS. This work shows great promise for accelerating tensor-valued dMRI to be translated in monitoring and predicting disease progression or evaluating treatment strategies in patients with MS.

Author contributions

YH and TBD designed the research, YH performed animal experiments, acquired and analyzed data, and YH, SA, HRS, and TBD interpreted the results and wrote the manuscript.

Funding

The authors disclosed receipt of the following financial support for the research, authorship, and publication of this article: This project has received funding from the European Union's Horizon 2020 research and innovation programme under the Marie Skłodowska-Curie Grant Agreement No. 843352; the Lundbeck Foundation (R287-2018-479). YH acknowledges support from the European Union's Horizon 2020 research and innovation programme under the Marie Skłodowska-Curie Grant Agreement No. 843352 and the Lundbeck Foundation (R287-2018-479). TD has received funding from the Capital Region Research Foundation (No. A5657). HRS holds a 5-year professorship in precision medicine at the Faculty of Health Sciences and Medicine, University of Copenhagen which is sponsored by the Lundbeckfonden (R186-2015-2138).

Declaration of Competing Interest

Hartwig R. Siebner has received honoraria as speaker from Sanofi Genzyme, Denmark and Novartis, Denmark, as consultant for Sanofi Genzyme, Denmark, Lophora, Denmark, and Lundbeck AS, Denmark, and as editor-in-chief (Neuroimage Clinical) and senior editor (NeuroImage) from Elsevier Publishers, Amsterdam, The Netherlands. He has received royalties as book editor from Springer Publishers, Stuttgart, Germany and from Gyldendal Publishers, Copenhagen, Denmark. The other authors report no conflict of interests.

Acknowledgments

The authors would like to thank Sascha Gude and Christian Skoven for their animal ethics and maintenance support. We also would like to thank Dr. Matthew D. Budde for providing free-waveform encoding EPI sequence. The authors are grateful to Susanne Sørensen for preparing the samples and conduction of the histological validation. We also thank Dr. Henrik Lundell for his suggestion and discussion on μFA calculation using the tuned LTE waveform.

Appendix A. Supplementary data

Supplementary data to this article can be found online at https://doi.org/10.1016/j.nicl.2021.102675.

References

Abdollahzadeh, A., Belevich, I., Jokitalo, E., Tohka, J., Sierra, A., 2019. Automated 3D axonal morphometry of white matter. Sci. Rep. 9, 6084.

Afzali, M., Aja-Fernández, S., Jones, D.K., 2020. Direction-averaged diffusion-weighted MRI signal using different axisymmetric B-tensor encoding schemes. Magn. Reson. Med. 84, 1579–1591.

Aharoni, R., Sasson, E., Blumenfeld-Katzir, T., Eilam, R., Sela, M., Assaf, Y., Arnon, R., 2013. Magnetic resonance imaging characterization of different experimental autoimmune encephalomyelitis models and the therapeutic effect of glatiramer acetate. Exp. Neurol. 240, 130–144.

Alexander, D.C., Dyrby, T.B., Nilsson, M., Zhang, H., 2019. Imaging brain microstructure with diffusion MRI: practicality and applications. NMR Biomed. 32, e3841.

Andersen, K.W., Lasič, S., Lundell, H., Nilsson, M., Topgaard, D., Sellebjerg, F., Szczepankiewicz, F., Siebner, H.R., Blinkenberg, M., Dyrby, T.B., 2020. Disentangling white-matter damage from physiological fiber orientation dispersion in multiple sclerosis. Brain Commn.

Andersson, M., Kjer, H.M., Rafael-Patino, J., Pacureanu, A., Pakkenberg, B., Thiran, J.-P., Ptito, M., Bech, M., Bjorholm Dahl, A., Andersen Dahl, V., Dyrby, T.B., 2020. Axon morphology is modulated by the local environment and impacts the noninvasive investigation of its structure–function relationship. Proc. Natl. Acad. Sci. 117, 33649.

Battini, S., Bund, C., Moussallieh, F., Çiçek, A., De Sèze, J., Namer, I., 2018. Metabolomics approaches in experimental allergic encephalomyelitis. J. Neuroimmunol. 314, 94–100.

Bester, M., Jensen, J., Babb, J., Tabesh, A., Miles, L., Herbert, J., Grossman, R., Inglese, M., 2015. Non-Gaussian diffusion MRI of gray matter is associated with cognitive impairment in multiple sclerosis. Multiple Sclerosis J. 21, 935–944.

Bitsch, A., Bruhn, H., Vougioukas, V., Stringaris, A., Lassmann, H., Frahm, J., Brück, W., 1999. Inflammatory CNS demyelination: histopathologic correlation with in vivo quantitative proton MR spectroscopy. Am. J. Neuroradiol. 20, 1619.

Brand, A., Richter-Landsberg, C., Leibfritz, D., 1993. Multinuclear NMR studies on the energy metabolism of glial and neuronal cells. Dev. Neurosci. 15, 289–298.

Calabrese, M., Magliozzi, R., Ciccarelli, O., Geurts, J.J., Reynolds, R., Martin, R., 2015. Exploring the origins of grey matter damage in multiple sclerosis. Nat. Rev. Neurosci. 16, 147–158.

Calabrese, M., Poretto, V., Favaretto, A., Alessio, S., Bernardi, V., Romualdi, C., Rinaldi, F., Perini, P., Gallo, P., 2012. Cortical lesion load associates with progression of disability in multiple sclerosis. Brain 135, 2952–2961.

Cardiff, R.D., Miller, C.H., Munn, R.J., 2014. Manual hematoxylin and eosin staining of mouse tissue sections. Cold Spring Harbor Protocols 655–658.

Chu, T., Zhang, Y.P., Tian, Z., Ye, C., Zhu, M., Shields, L.B.E., Kong, M., Barnes, G.N., Shields, C.B., Cai, J., 2019. Dynamic response of microglia/macrophage polarization following demyelination in mice. J. Neuroinflammation 16, 188.

Chuhutin, A., Hansen, B., Wlodarczyk, A., Owens, T., Shemesh, N., Jespersen, S.N., 2019. Diffusion Kurtosis Imaging maps neural damage in the EAE model of multiple sclerosis. NeuroImage 116406.

Corral, M.A.P., Govindarajan, S.T., Stefancin, P., Bangiyev, L., Coyle, P.K., Duong, T.Q., 2019. Characterization of gray-matter multiple sclerosis lesions using double inversion recovery, diffusion, contrast-enhanced, and volumetric MRI. Multiple Sclerosis Related Disorders 31, 74–81.

Correale, J., Gaitán, M.I., Ysrraelit, M.C., Fiol, M.P., 2017. Progressive multiple sclerosis: from pathogenic mechanisms to treatment. Brain 140, 527–546.

Davie, C., Hawkins, C., Barker, G., Brennan, A., Tofts, P., Miller, D., McDonald, W., 1994. Serial proton magnetic resonance spectroscopy in acute multiple sclerosis lesions. Brain 117, 49–58.

DeBoy, C.A., Zhang, J., Dike, S., Shats, I., Jones, M., Reich, D.S., Mori, S., Nguyen, T., Rothstein, B., Miller, R.H., Griffin, J.T., Kerr, D.A., Calabresi, P.A., 2007. High resolution diffusion tensor imaging of axonal damage in focal inflammatory and demyelinating lesions in rat spinal cord. Brain 130, 2199–2210.

Degaonkar, M.N., Jayasundar, R., Jagannathan, N.R., 2002. Sequential diffusion-weighted magnetic resonance imaging study of lysophosphatidyl choline-induced experimental demyelinating lesion: An animal model of multiple sclerosis. J. Magn. Reson. Imaging 16, 153–159.

Dousset, V., Brochet, B., Vital, A., Gross, C., Benazzouz, A., Boullerne, A., Bidabe, A.-M., Gin, A.-M., Caille, J.-M., 1995. Lysolecithin-induced demyelination in primates: preliminary in vivo study with MR and magnetization transfer. Am. J. Neuroradiol. 16, 225–231.

Edén, M., 2003. Computer simulations in solid-state NMR. III. Powder averaging. Concepts Magnet. Resonance Part A 18A, 24–55.

Fleischer, V., Kolb, R., Groppa, S., Zipp, F., Klose, U., Gröger, A., 2016. Metabolic patterns in chronic multiple sclerosis lesions and normal-appearing white matter: intraindividual comparison by using 2D MR spectroscopic imaging. Radiology 281, 536–543.

Fujiyoshi, K., Hikishima, K., Nakahara, J., Tsuji, O., Hata, J., Konomi, T., Nagai, T., Shibata, S., Kaneko, S., Iwanami, A., Momoshima, S., Takahashi, S., Jinzaki, M., Suzuki, N., Toyama, Y., Nakamura, M., Okano, H., 2016. Application of q-space diffusion MRI for the visualization of white matter. J. Neurosci. 36, 2796.

Ghasemlou, N., Jeong, S.Y., Lacroix, S., David, S., 2007. T cells contribute to lysophosphatidylcholine-induced macrophage activation and demyelination in the CNS. Glia 55, 294–302.

Gochberg, D.F., Gore, J.C., 2007. Quantitative magnetization transfer imaging via selective inversion recovery with short repetition times. Magnetic Resonance Med. 57, 437–441.

Guglielmetti, C., Veraart, J., Roelant, E., Mai, Z., Daans, J., Van Audekerke, J., Naeyaert, M., Vanhoutte, G., y Palacios, R.D., Praet, J., 2016. Diffusion kurtosis imaging probes cortical alterations and white matter pathology following cuprizone induced demyelination and spontaneous remyelination. NeuroImage 125, 363–377.

Haider, L., Simeonidou, C., Steinberger, G., Hametner, S., Grigoriadis, N., Deretzi, G., Kovacs, G.G., Kutzelnigg, A., Lassmann, H., Frischer, J.M., 2014. Multiple sclerosis deep grey matter: the relation between demyelination, neurodegeneration, inflammation and iron. J. Neurol. Neurosurg. Psychiatry 85, 1386–1395.

He, Y., Wang, M., Chen, X., Pohmann, R., Polimeni, J.R., Scheffler, K., Rosen, B.R., Kleinfeld, D., Yu, X., 2018. Ultra-slow single-vessel BOLD and CBV-based fMRI spatiotemporal dynamics and their correlation with neuronal intracellular calcium signals. Neuron 97 (925–939), e925.

Heath, F., Hurley, S.A., Johansen-Berg, H., Sampaio-Baptista, C., 2018. Advances in noninvasive myelin imaging. Dev. Neurobiol. 78, 136–151.

Helms, G., Dathe, H., Kallenberg, K., Dechent, P., 2008. High-resolution maps of magnetization transfer with inherent correction for RF inhomogeneity and T1 relaxation obtained from 3D FLASH MRI. Magn. Reson. Med. 60, 1396–1407.

Hnilicová, P., Kantorová, E., Poláček, H., Grendár, M., Bittšanský, M., Čierny, D., Sivák, Š., Zeleňák, K., Lehotský, J., Dobrota, D., 2019. Altered hypothalamic metabolism in early multiple sclerosis–MR spectroscopy study. J. Neurol. Sci. 407, 116458.

Ineichen, B.V., Sati, P., Granberg, T., Absinta, M., Lee, N.J., Lefeuvre, J.A., Reich, D.S., 2020. Magnetic resonance imaging in multiple sclerosis animal models: A systematic review, meta-analysis, and white paper. NeuroImage: Clinical 28, 102371.

Jeffery, N.D., Blakemore, W.F., 1995. Remyelination of mouse spinal cord axons demyelinated by local injection of lysolecithin. J. Neurocytol. 24, 775–781.

Jelescu, I.O., Zurek, M., Winters, K.V., Veraart, J., Rajaratnam, A., Kim, N.S., Babb, J.S., Shepherd, T.M., Novikov, D.S., Kim, S.G., Fieremans, E., 2016. In vivo quantification of demyelination and recovery using compartment-specific diffusion MRI metrics validated by electron microscopy. NeuroImage 132, 104–114.

Jespersen, S.N., Lundell, H., Sønderby, C.K., Dyrby, T.B., 2013. Orientationally invariant metrics of apparent compartment eccentricity from double pulsed field gradient diffusion experiments. NMR Biomed. 26, 1647–1662.

Jespersen, S.N., Lundell, H., Sønderby, C.K., Dyrby, T.B., 2014. Commentary on "Microanisotropy imaging: quantification of microscopic diffusion anisotropy and orientation of order parameter by diffusion MRI with magic-angle spinning of the q-vector". Front. Phys. 2, 28.

Jones, D.K., 2004. The effect of gradient sampling schemes on measures derived from diffusion tensor MRI: a Monte Carlo study. Magn. Reson. Med. 51, 807–815.

Jones, D.K., Basser, P.J., 2004. "Squashing peanuts and smashing pumpkins": how noise distorts diffusion-weighted MR data. Magn. Reson. Med. 52, 979–993.

Jones, D.K., Horsfield, M.A., Simmons, A., 1999. Optimal strategies for measuring diffusion in anisotropic systems by magnetic resonance imaging. Magn. Reson. Med. 42, 515–525.

Kaden, E., Kelm, N.D., Carson, R.P., Does, M.D., Alexander, D.C., 2016. Multi-compartment microscopic diffusion imaging. NeuroImage 139, 346–359.

Kerkelä, L., Henriques, R.N., Hall, M.G., Clark, C.A., Shemesh, N., 2020. Validation and noise robustness assessment of microscopic anisotropy estimation with clinically feasible double diffusion encoding MRI. Magn. Reson. Med. 83, 1698–1710.

Lampinen, B., Szczepankiewicz, F., Mårtensson, J., van Westen, D., Sundgren, P.C., Nilsson, M., 2017. Neurite density imaging versus imaging of microscopic anisotropy in diffusion MRI: A model comparison using spherical tensor encoding. NeuroImage 147, 517–531.

Lasič, S., Szczepankiewicz, F., Eriksson, S., Nilsson, M., Topgaard, D., 2014. Microanisotropy imaging: quantification of microscopic diffusion anisotropy and orientational order parameter by diffusion MRI with magic-angle spinning of the q-vector. Front. Phys. 2, 11.

Lassmann, H., Bradl, M., 2017. Multiple sclerosis: experimental models and reality. Acta Neuropathol. 133, 223–244.

Lau, L.W., Keough, M.B., Haylock-Jacobs, S., Cua, R., Döring, A., Sloka, S., Stirling, D.P., Rivest, S., Yong, V.W., 2012. Chondroitin sulfate proteoglycans in demyelinated lesions impair remyelination. Ann. Neurol. 72, 419–432.

Lawrenz, M., Finsterbusch, J., 2019. Detection of microscopic diffusion anisotropy in human cortical gray matter in vivo with double diffusion encoding. Magn. Reson. Med. 81, 1296–1306.

Le Bihan, D., Johansen-Berg, H., 2012. Diffusion MRI at 25: Exploring brain tissue structure and function. NeuroImage 61, 324–341.

Lee, H.-H., Jespersen, S.N., Fieremans, E., Novikov, D.S., 2020. The impact of realistic axonal shape on axon diameter estimation using diffusion MRI. NeuroImage 117228.

Lehto, L.J., Albors, A.A., Sierra, A., Tolppanen, L., Eberly, L.E., Mangia, S., Nurmi, A., Michaeli, S., Gröhn, O., 2017. Lysophosphatidyl choline induced demyelination in rat probed by relaxation along a fictitious field in high rank rotating frame. Front. Neurosci. 11, 433.

Lipp, I., Parker, G.D., Tallantyre, E.C., Goodall, A., Grama, S., Patitucci, E., Heveron, P., Tomassini, V., Jones, D.K., 2020. Tractography in the presence of multiple sclerosis lesions. NeuroImage 209, 116471.

Lundell, H., Nilsson, M., Dyrby, T., Parker, G., Cristinacce, P.H., Zhou, F.-L., Topgaard, D., Lasič, S., 2019. Multidimensional diffusion MRI with spectrally modulated gradients reveals unprecedented microstructural detail. Sci. Rep. 9, 9026.

Luo, T., Oladosu, O., Rawji, K.S., Zhai, P., Pridham, G., Hossain, S., Zhang, Y., 2019. Characterizing structural changes with evolving remyelination following experimental demyelination using high angular resolution diffusion MRI and texture analysis. J. Magn. Reson. Imaging 49, 1750–1759.
McClymont, D., Teh, I., Schneider, J.E., 2017. The impact of signal-to-noise ratio, diffusion-weighted directions and image resolution in cardiac diffusion tensor imaging – insights from the ex-vivo rat heart. J. Cardiovasc. Magn. Reson. 19, 90.
McCreary, C.R., Bjarnason, T.A., Skihar, V., Mitchell, J.R., Yong, V.W., Dunn, J.F., 2009. Multiexponential T2 and magnetization transfer MRI of demyelination and remyelination in murine spinal cord. NeuroImage 45, 1173–1182.
McKeithan, L.J., Lyttle, B.D., Box, B.A., O'Grady, K.P., Dortch, R.D., Conrad, B.N., Thompson, L.M., Rogers, B.P., Newhouse, P., Pawate, S., 2019. 7T quantitative magnetization transfer (qMT) of cortical gray matter in multiple sclerosis correlates with cognitive impairment. NeuroImage 203, 116190.
McMurray, H.F., Parthasarathy, S., Steinberg, D., 1993. Oxidatively modified low density lipoprotein is a chemoattractant for human T lymphocytes. J. Clin. Investig. 92, 1004–1008.
Moffett, J.R., Ross, B., Arun, P., Madhavarao, C.N., Namboodiri, A.M.A., 2007. N-Acetylaspartate in the CNS: from neurodiagnostics to neurobiology. Prog. Neurobiol. 81, 89–131.
Nathoo, N., Yong, V.W., Dunn, J.F., 2014. Understanding disease processes in multiple sclerosis through magnetic resonance imaging studies in animal models. NeuroImage: Clinical 4, 743–756.
Nilsson, M., Szczepankiewicz, F., Brabec, J., Taylor, M., Westin, C.-F., Golby, A., van Westen, D., Sundgren, P.C., 2020. Tensor-valued diffusion MRI in under 3 minutes: an initial survey of microscopic anisotropy and tissue heterogeneity in intracranial tumors. Magn. Reson. Med. 83, 608–620.
Novikov, D.S., Fieremans, E., Jespersen, S.N., Kiselev, V.G., 2019. Quantifying brain microstructure with diffusion MRI: Theory and parameter estimation. NMR Biomed. 32, e3998.
Oakden, W., Bock, N.A., Al-Ebraheem, A., Farquharson, M.J., Stanisz, G.J., 2017. Early regional cuprizone-induced demyelination in a rat model revealed with MRI. NMR Biomed. 30.
Orije, J., Kara, F., Guglielmetti, C., Praet, J., Van der Linden, A., Ponsaerts, P., Verhoye, M., 2015. Longitudinal monitoring of metabolic alterations in cuprizone mouse model of multiple sclerosis using 1H-magnetic resonance spectroscopy. NeuroImage 114, 128–135.
Plemel, J.R., Michaels, N.J., Weishaupt, N., Caprariello, A.V., Keough, M.B., Rogers, J.A., Yukseloglu, A., Lim, J., Patel, V.V., Rawji, K.S., 2018. Mechanisms of lysophosphatidylcholine-induced demyelination: A primary lipid disrupting myelinopathy. Glia 66, 327–347.
Provencher, S.W., 2001. Automatic quantitation of localized in vivo 1H spectra with. LCModel. 14, 260–264.
Quinn, M.T., Parthasarathy, S., Steinberg, D., 1988. Lysophosphatidylcholine: a chemotactic factor for human monocytes and its potential role in atherogenesis. Proc. Natl. Acad. Sci. 85, 2805.
Ransohoff, R.M., 2012. Animal models of multiple sclerosis: the good, the bad and the bottom line. Nat. Neurosci. 15, 1074–1077.
Reich, D.S., Lucchinetti, C.F., Calabresi, P.A., 2018. Multiple Sclerosis. N Engl J Med 378, 169–180.
Shemesh, N., 2018. Axon diameters and myelin content modulate microscopic fractional anisotropy at short diffusion times in fixed rat spinal cord. Front. Phys. 6, 49.
Shi, Y., Shao, Q., Li, Z., Gonzalez, G.A., Lu, F., Wang, D., Pu, Y., Huang, A., Zhao, C., He, C., Cao, L., 2018. Myt1L promotes differentiation of oligodendrocyte precursor cells and is necessary for remyelination after lysolecithin-induced demyelination. Neuroscience Bulletin 34, 247–260.
Szczepankiewicz, F., Lasič, S., van Westen, D., Sundgren, P.C., Englund, E., Westin, C.-F., Ståhlberg, F., Lätt, J., Topgaard, D., Nilsson, M., 2015. Quantification of microscopic diffusion anisotropy disentangles effects of orientation dispersion from microstructure: applications in healthy volunteers and in brain tumors. NeuroImage 104, 241–252.
Szczepankiewicz, F., Sjölund, J., Ståhlberg, F., Lätt, J., Nilsson, M., 2019. Tensor-valued diffusion encoding for diffusional variance decomposition (DIVIDE): Technical feasibility in clinical MRI systems. PLoS ONE 14, e0214238.
Szczepankiewicz, F., van Westen, D., Englund, E., Westin, C.-F., Ståhlberg, F., Lätt, J., Sundgren, P.C., Nilsson, M., 2016. The link between diffusion MRI and tumor heterogeneity: Mapping cell eccentricity and density by diffusional variance decomposition (DIVIDE). NeuroImage 142, 522–532.
Thompson, A.J., Banwell, B.L., Barkhof, F., Carroll, W.M., Coetzee, T., Comi, G., Correale, J., Fazekas, F., Filippi, M., Freedman, M.S., Fujihara, K., Galetta, S.L., Hartung, H.P., Kappos, L., Lublin, F.D., Marrie, R.A., Miller, A.E., Miller, D.H., Montalban, X., Mowry, E.M., Sorensen, P.S., Tintoré, M., Traboulsee, A.L., Trojano, M., Uitdehaag, B.M.J., Vukusic, S., Waubant, E., Weinshenker, B.G., Reingold, S.C., Cohen, J.A., 2018. Diagnosis of multiple sclerosis: 2017 revisions of the McDonald criteria. Lancet Neurol. 17, 162–173.
Tourdias, T., Mori, N., Dragonu, I., Cassagno, N., Boiziau, C., Aussudre, J., Brochet, B., Moonen, C., Petry, K.G., Dousset, V., 2011. Differential aquaporin 4 expression during edema build-up and resolution phases of brain inflammation. J. Neuroinflammation 8, 143.
Turati, L., Moscatelli, M., Mastropietro, A., Dowell, N.G., Zucca, I., Erbetta, A., Cordiglieri, C., Brenna, G., Bianchi, B., Mantegazza, R., Cercignani, M., Baggi, F., Minati, L., 2015. In vivo quantitative magnetization transfer imaging correlates with histology during de- and remyelination in cuprizone-treated mice 28, 327–337.
West, K.L., Kelm, N.D., Carson, R.P., Gochberg, D.F., Ess, K.C., Does, M.D., 2018. Myelin volume fraction imaging with MRI. NeuroImage 182, 511–521.
Westin, C.F., Knutsson, H., Pasternak, O., Szczepankiewicz, F., Ozarslan, E., van Westen, D., Mattisson, C., Bogren, M., O'Donnell, L.J., Kubicki, M., Topgaard, D., Nilsson, M., 2016. Q-space trajectory imaging for multidimensional diffusion MRI of the human brain. NeuroImage 135, 345–362.
Yablonskiy, D.A., Sukstanskii, A.L., Leawoods, J.C., Gierada, D.S., Bretthorst, G.L., Lefrak, S.S., Cooper, J.D., Conradi, M.S., 2002. Quantitative in vivo assessment of lung microstructure at the alveolar level with hyperpolarized ³He diffusion MRI. Proc. Natl. Acad. Sci. 99, 3111.
Yazdi, A., Baharvand, H., Javan, M., 2015. Enhanced remyelination following lysolecithin-induced demyelination in mice under treatment with fingolimod (FTY720). Neuroscience 311, 34–44.
Yon, M., de Almeida Martins, J.P., Bao, Q., Budde, M.D., Frydman, L., Topgaard, D., 2020. Diffusion tensor distribution imaging of an in vivo mouse brain at ultrahigh magnetic field by spatiotemporal encoding. NMR in Biomedicine 33, e4355. https://doi.org/10.1002/nbm.4355.
Zhang, H., Schneider, T., Wheeler-Kingshott, C.A., Alexander, D.C., 2012. NODDI: practical in vivo neurite orientation dispersion and density imaging of the human brain. NeuroImage 61, 1000–1016.